Realizing High Thermoelectric Performance in n-Type Se-Free Bi_2Te_3 Materials by Spontaneous Incorporation of $FeTe_2$ Nanoinclusions

Jamil Ur Rahman, Woo Hyun Nam, Yong-Jae Jung, Jong Ho Won, Jong-Min Oh, Nguyen Van Du, Gul Rahman, Víctor M. García-Suárez, Ran He, Kornelius Nielsch, Jung Young Cho, Won-Seon Seo, Jong Wook Roh, Sang-il Kim ⓘ, Soonil Lee, Kyu Hyoung Lee*, Hyun Sik Kim*, and Weon Ho Shin* ⓘ

Bi_2Te_3-based materials have drawn much attention from the thermoelectric community due to their excellent thermoelectric performance near room temperature. However, the stability of existing n-type $Bi_2(Te,Se)_3$ materials is still low due to the evaporation energy of Se (37.70 kJ mol^{-1}) being much lower than that of Te (52.55 kJ mol^{-1}). The evaporated Se from the material causes problems in interconnects of the module while degrading the efficiency. Here, we have developed a new approach for the high-performance and stable n-type Se-free Bi_2Te_3-based materials by maximizing the electronic transport while suppressing the phonon transport, at the same time. Spontaneously generated $FeTe_2$ nanoinclusions within the matrix during the melt-spinning and subsequent spark plasma sintering is the key to simultaneous engineering of the power factor and lattice thermal conductivity. The nanoinclusions change the fermi level of the matrix while intensifying the phonon scattering via nanoparticles. With a fine-tuning of the fermi level with Cu doping in the n-type Bi_2Te_3–$0.02FeTe_2$, a high power factor of $\sim 41 \times 10^{-4}$ Wm^{-1} K^{-2} with an average zT of 1.01 at the temperature range 300–470 K are achieved, which are comparable to those obtained in n-type $Bi2(Te,Se)_3$ materials. The proposed approach enables the fabrication of high-performance n-type Bi_2Te_3-based materials without having to include volatile Se element, which guarantees the stability of the material. Consequently, widespread application of thermoelectric devices utilizing the n-type Bi_2Te_3-based materials will become possible.

1. Introduction

Thermoelectric (TE) technology takes advantage of a temperature gradient to enable the waste heat energy from power plants and vehicles to be converted into useful electrical energy. The unique features of TE technology, such as stability and portability, make it suitable for various applications in different fields. From space missions to industrial waste heat recovery systems, TE devices are helping to increase efficiency and reduce energy costs.[1,2] Powering remote sensors and coolers for temperature-controlled drug delivery systems make TE devices ideal for applications in industries.[3–6] The performance of TE materials depends on the dimensionless figure-of-merit $zT = \sigma S^2 T/\kappa_{tot}$, where S, σ, κ_{tot}, and T are the Seebeck coefficient, electrical conductivity, total thermal conductivity, and absolute temperature, respectively.[7–10] Moreover, κ_{tot} consists of two terms, namely the lattice thermal conductivity (κ_{lat}) and electronic thermal conductivity (κ_{ele}). The κ_{ele} is calculated using the Wiedemann-Franz law $\kappa_{ele} = L\sigma T$, where L is the Lorenz number.[11–14] To enhance the performance of a TE material, i.e.,

Dr. J. U. Rahman, Dr. R. He, Dr. K. Nielsch
Leibniz Institute for Solid State and Materials Research, Dresden 01069, Germany
Dr. W. H. Nam, Dr. J. Y. Cho
Advanced Materials Convergence R&D Division, Korea Institute of Ceramic Engineering & Technology, Jinju 52861, South Korea
Y.-J. Jung, Prof. J.-M. Oh, Prof. W. H. Shin
Department of Electronic Materials Engineering, Kwangwoon University, Seoul 01897, South Korea
E-mail: weonho@kw.ac.kr
Prof. J. H. Won
Department of Energy Engineering, Dankook University, Cheonan 31116, South Korea
Prof. N. Van Du
Faculty of Fundamental Science, Phenikaa University, Hanoi 10000, Vietnam
Prof. G. Rahman
Department of Physics, Quaid-i-Azam University, Islamabad 45320, Pakistan
Prof. V. M. García-Suárez
Departamento de Física, Universidad de Oviedo, Oviedo 33007, Spain
Prof. V. M. García-Suárez
Nanomaterials and Nanotechnology Research Center-CINN, El Entrego 33940, Spain

Dr. W.-S. Seo, Prof. K. H. Lee
Department of Materials Science and Engineering, Yonsei University, Seoul 03722, South Korea
E-mail: khlee2018@yonsei.ac.kr
Prof. J. W. Roh
School of Nano & Materials Science and Engineering, Kyungpook National University, Sangju 37224, South Korea
Prof. S.-i. Kim, Prof. H. S. Kim
Department of Materials Science and Engineering, University of Seoul, Seoul 02504, South Korea
E-mail: hyunsik.kim@uos.ac.kr
Prof. S. Lee
School of Materials Science and Engineering, Changwon National University, Changwon 51140, South Korea
ⓘ The ORCID identification number(s) for the author(s) of this article can be found under https://doi.org/10.1002/eem2.12663.

Correction added on 31st August 2023, after the first online publication Figure 6 has been updated.

maximize zT, it is necessary to increase the power factor (PF, σS^2) and concomitantly reduce the κ_{lat}. Controlling these three parameters (σ, S, κ_{tot}) independently is the key strategy for attaining high zT. Bismuth telluride (Bi_2Te_3) and its alloys with Bi_2Se_3 or Sb_2Te_3 rank among the most important classes of TE materials and are widely used in applications operating near room temperature.[15,16]

Introducing defects into the Bi_2Te_3 matrix has been intensively researched as an effective way to enhance the TE performance. For instance, in the case of native defects in Bi_2Te_3, the Te vacancy (V_{Te}) and antisite defect (Te_{Bi}) act as donor-like defects that provide n-type conduction. On the other hand, the Bi-vacancy (V_{Bi}) and antisite defect (Bi_{Te}) are acceptor-like defects that enhance p-type conduction. In addition, several other strategies have been developed to improve the TE performance of Bi_2Te_3-based materials, either by enhancing the PF through band convergence, low-energy carrier filtering, and doping, or by reducing κ_{lat} by introducing nanosized grain boundaries, dislocation arrays, and nanoinclusions.[16–25] Among them, the nano-inclusion approach is coming to the pioneering way in terms of their exceptional enhancement of S value as well as encouraging phonon scattering. However, most of the works use additional processes to synthesize certain nanoparticle structure,[20,22,25] which is not suitable for mass production.

It is commonly believed that alloying Bi_2Te_3 with isostructural Sb_2Te_3 improves p-type conduction by band-structure modification and additional defect scattering of phonons, which has been shown to achieve a very high $zT \sim 1.86$ at 320 K.[16] Similarly, alloying Bi_2Te_3 with isostructural Bi_2Se_3 enhances n-type conduction by lowering the formation energy of anion vacancies (V_{Bi}, V_{Sb}). Nevertheless, the improvement in zT of n-type $Bi_2(Te_xSe_{1-x})_3$ has fallen behind the advances made in its p-type counterpart and has remained a challenge over the past 50 years, for both single-crystal and polycrystalline bulk materials; this has seriously restricted the development of high-performance TE modules.[26–30] A recent study demonstrated a significant improvement of n-type TE performance in $Bi_{1.8}Sb_{0.2}Te_{2.7}Se_{0.3}$, via the introduction of dislocation arrays that provide an outstanding zT value of 1.4 at 420 K.[31] However, the typical problem with n-type $Bi_2(Te_xSe_{1-x})_3$ alloys is the lack of stability and reproducibility, which is related to the evaporation of Se atoms at elevated temperature, i.e., changes in the nominal stoichiometry of $Bi_2(Te_xSe_{1-x})_3$ that affect the overall TE properties.[29,32] Over the past decade it was tested and developed by the 3 M Corporation, at the National Aeronautics and Space Administration (NASA) Jet Propulsion Laboratory, Teledyne Energy Systems, and the General Atomics Corporation for use as a next-generation thermoelectric material. During these tests, the evaporated Se atoms at working temperature and their reaction with other components of electronic devices cause a significant problem in the electrical interconnects or operating devices.[33,34] Such conditions also result in the physical separation of material from the electrical contacts of the device.[35,36] To mitigate this problem, it is highly desirable to develop Se-free Bi_2Te_3 alloys with n-type conduction that have high zT comparable to their p-type counterparts.

Herein, we propose a novel approach to optimize the zT of n-type Se-free Bi_2Te_3-based alloys that is comparable to its p-type counterpart. First, we pursue the strategy of inducing $FeTe_2$ nanoprecipitates spontaneously using melt spinning (MS) and spark plasma sintering (SPS), i.e., the incorporation of a certain fraction of selected elements to distort the lattice, thereby enhancing electrical properties and phonon scattering as well. After that, a foreign element acting as a compensating acceptor (Cu) was introduced to optimize the carrier concentration to

maximize the PF. The remarkable advantage of this strategy is that $FeTe_2$ precipitates scatter the phonons, which results in low κ_{lat} with high PF, and the Cu atoms independently control the carrier concentration. This strategy significantly enhanced the maximum TE figure of merit (zT_{max}) by more than 60%, i.e., from ~ 0.68 (Bi_2Te_3) to ~ 1.08 (Bi_2Te_3–$0.02FeTe_2$–0.0125Cu), while achieving a Se-free n-type Bi_2Te_3-based TE material. Furthermore, the $FeTe_2$ incorporation does not need any additional process, which is thought to be a significant advantage for cost-effective production.

2. Results and Discussion

2.1. Structural Characterization of Bi_2Te_3-$xFeTe_2$

First, we prepared the $FeTe_2$-incorporated Bi_2Te_3 samples by MS and SPS methods. **Figure 1** shows XRD patterns of bulk Bi_2Te_3-$xFeTe_2$ ($x = 0$, 0.01, 0.02, 0.03, and 0.04) samples. The main diffraction peaks correspond to the rhombohedral Bi_2Te_3 structure (JCPDS # 65-3674). The relative peak intensities are the same for all samples, indicating there is no specific orientation. It is noteworthy that small peaks of $FeTe_2$ (JCPDS #14-0419) are also present in addition to the main crystal peaks of Bi_2Te_3, and the intensity of the $FeTe_2$ peaks systematically increases with increasing $FeTe_2$ content. Regarding the atomic radius differences between the Fe (1.35 Å) and Bi atoms (1.60 Å),[37] Fe doping on Bi-sites does not seem probable. Still, there are a few reports that demonstrate Fe doping on the Bi-site of Bi_2Te_3.[38,39] The reason that the $FeTe_2$ nanoparticle precipitates instead of doping may be related to the MS process we adopted to maximize the cooling rate of the melt ingots and subsequent spark plasma sintering.[40]

To understand the microstructure of the $FeTe_2$ phase in Bi_2Te_3, transmission electron microscopy (TEM) observations were conducted over the Bi_2Te_3–$xFeTe_2$ samples. **Figure 2** shows representative TEM images for $x = 0.02$ (which has the optimized transport properties, see below). $FeTe_2$ phase is found to distribute in the Bi_2Te_3 grain with an
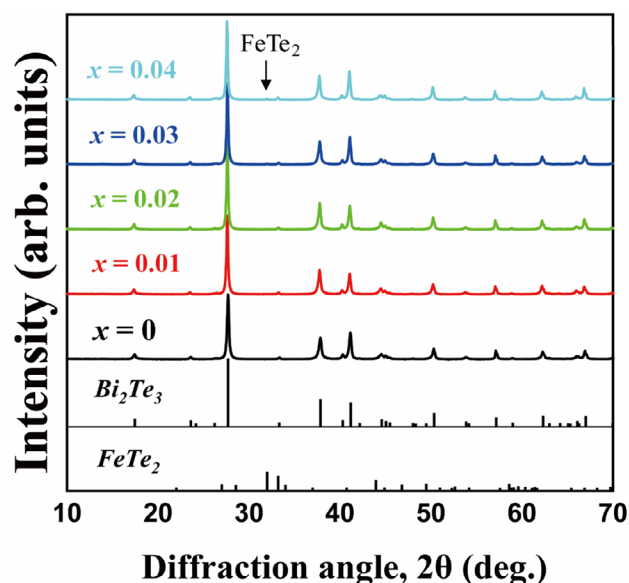

Figure 1. XRD patterns of the Bi_2Te_3–$xFeTe_2$ samples ($x = 0$–0.04).

average size of less than 300 nm, as indicated by the red arrow in the TEM image in Figure 2a. In addition to the $FeTe_2$ phase, several darker-contrast nano-precipitates were also observed, as indicated by the yellow arrow in the high-angle annular dark field (HAADF) image. This $FeTe_2$ phase and dark-contrast nano-precipitates were selected for further analysis of their structures and chemical compositions. The results are shown as HAADF images, energy-dispersive X-ray spectroscopy (EDS) maps, and high-resolution TEM (HRTEM) in Figure 2b–e. The round particles in the HAADF image with lighter contrast in comparison with the Bi_2Te_3 matrix are identified as $FeTe_2$, which is consistent with the XRD data, while the nano-precipitates (<50 nm in size) are probably $FeTe_{0.9}$ (Fe-rich phase). The high-resolution TEM (HRTEM) images and selected area electron diffraction (SAED) patterns confirms the phase and stoichiometry at the nanoscale, i.e., $FeTe_2$ and $FeTe_{0.9}$ phases (Figure 2f,g). Lastly, the geometric phase analysis (GPA) was carried out on the HRTEM image of the $Bi_2Te_3/FeTe_2$ interface in Bi_2Te_3–$0.02FeTe_2$ (Figure S8, Supporting Information) to investigate the local lattice distortion in the Bi_2Te_3 matrix caused by the incorporation of $FeTe_2$ nanoprecipitates. The GPA result in Figure S8b, Supporting Information, confirms the presence of a noticeable strain field within the Bi_2Te_3 matrix adjacent to the $FeTe_2$ nanoprecipitate. The X-ray photoelectron spectroscopy (XPS) analysis conducted on the synthesized nanoinclusions revealed important information about their chemical state. Figure S11, Supporting Information, displays the Fe 2p

detailed spectra of the Bi_2Te_3–$0.02FeTe_2$ materials, which confirms the presence of two distinct phases, $FeTe_2$ and $FeTe_{0.9}$, within the composite structure, as shown on TEM observation. According to the XPS results, the amount of $FeTe_2$ is approximately 2.7 times higher than that of $FeTe_{0.9}$ in the composite material. This finding suggests that $FeTe_2$ is the predominant phase, constituting the majority of the synthesized nanoinclusions, while $FeTe_{0.9}$ represents a smaller portion. (see Supporting Information for more details). It is important to note that these nano-precipitates are spontaneously generated while undergoing MS and SPS processes. In other words, theses nano-precipitates are byproducts from MS and SPS of Bi_2Te_3–$xFeTe_2$ (x = 0, 0.01, 0.02, 0.03, and 0.04) ingots.

To more closely investigate the atomic arrangement of the nano-precipitates in Bi_2Te_3, we performed density functional theory calculations; we considered tetragonal FeTe and calculated its cohesive energy, and compared it with that of $FeTe_2$. The cohesive energies of $FeTe_2$ and FeTe are −4.79 and −4.86 eV which are very similar. These calculations indicate that the nano-precipitates observed in the EDS data could be tetragonal FeTe. The Fe-rich nano-precipitates ($FeTe_{0.9}$) can be simulated by reducing the content of Te in FeTe, as realized by considering a single Te vacancy in a $2 \times 2 \times 2$ supercell $Fe_{16}Te_{16}$ ($Fe_{16}Te_{15} \sim FeTe_{0.93}$). The cohesive energy of tetragonal $FeTe_{0.93}$ is −4.71 eV, which is close to that of $FeTe_2$. The electronic structure shows that $FeTe_{0.9}$ is metallic, unlike $FeTe_2$, which is a semiconductor.

Consequently, we successfully realized $FeTe_2$ nanoinclusions incorporated Bi_2Te_3 composite structure, where the $FeTe_2$ nanoinclusions are spontaneously generated during the Bi_2Te_3 matrix materials without any additional process.

2.2. Electrical Properties of Bi_2Te_3–$xFeTe_2$

Figure 3a displays the temperature-dependent σ of Bi_2Te_3-$xFeTe_2$ (x = 0, 0.01, 0.02, 0.03, and 0.04). The σ of the samples decreases slightly with increasing $FeTe_2$ content. In addition, the σ decreases with increasing temperature, suggesting typical heavily-doped semiconducting behavior. To understand the effects of $FeTe_2$ in Bi_2Te_3, temperature-dependent Hall effect measurements were performed. Interestingly, with the addition of $FeTe_2$ to the Bi_2Te_3 matrix, the carrier concentrations slightly decreased over the whole temperature range without affecting the carrier mobility, as shown in Figure 3b,c. The Hall measurement results imply that the decrease in σ is due to the decrease in the carrier concentration, rather than the carrier mobility. The decrease in the carrier concentrations is most likely due to band-structure modification rather than Fe doping of Bi_2Te_3. This implies that the addition of $FeTe_2$ nano inclusions modifies the electronic band structure of the Bi_2Te_3 matrix material by creating defects or impurities in the crystal lattice. These defects or impurities introduce additional energy states within
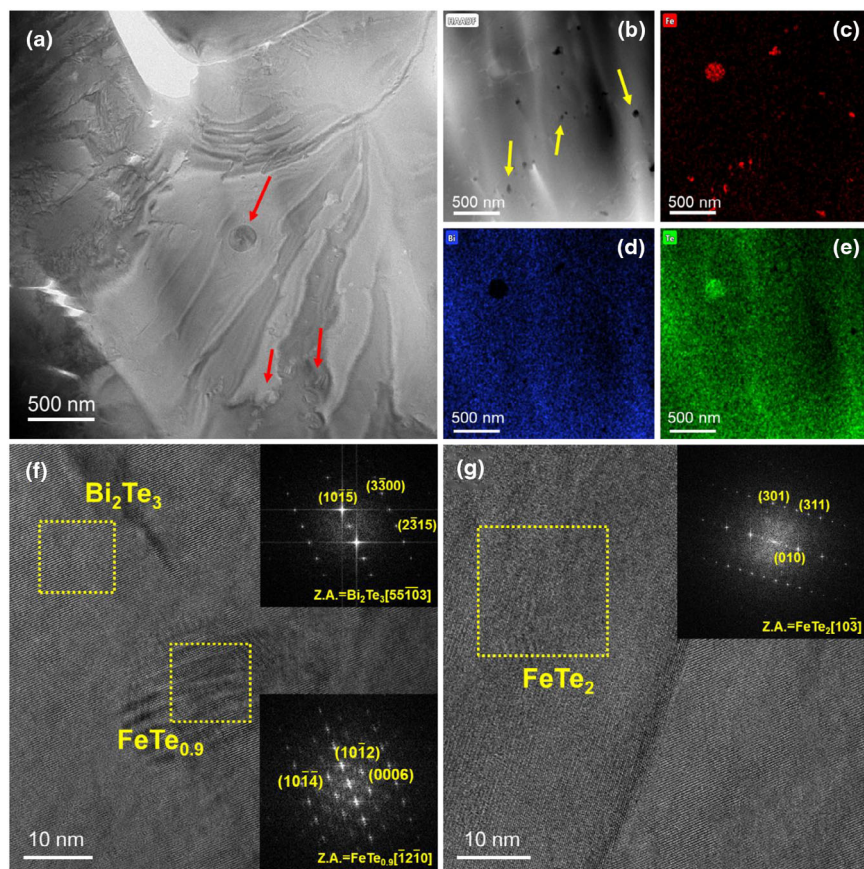

Figure 2. a) Low-magnification TEM image of Bi_2Te_3–$0.02FeTe_2$. b) HADDF image of Bi_2Te_3–$0.02FeTe_2$. EDS elemental maps for c) Fe, d) Bi, and e) Te. f, g) HRTEM images of Bi_2Te_3 matrix and precipitates in the Bi_2Te_3–$0.02FeTe_2$ sample. (inset images) Corresponding diffraction patterns of the selected parts.
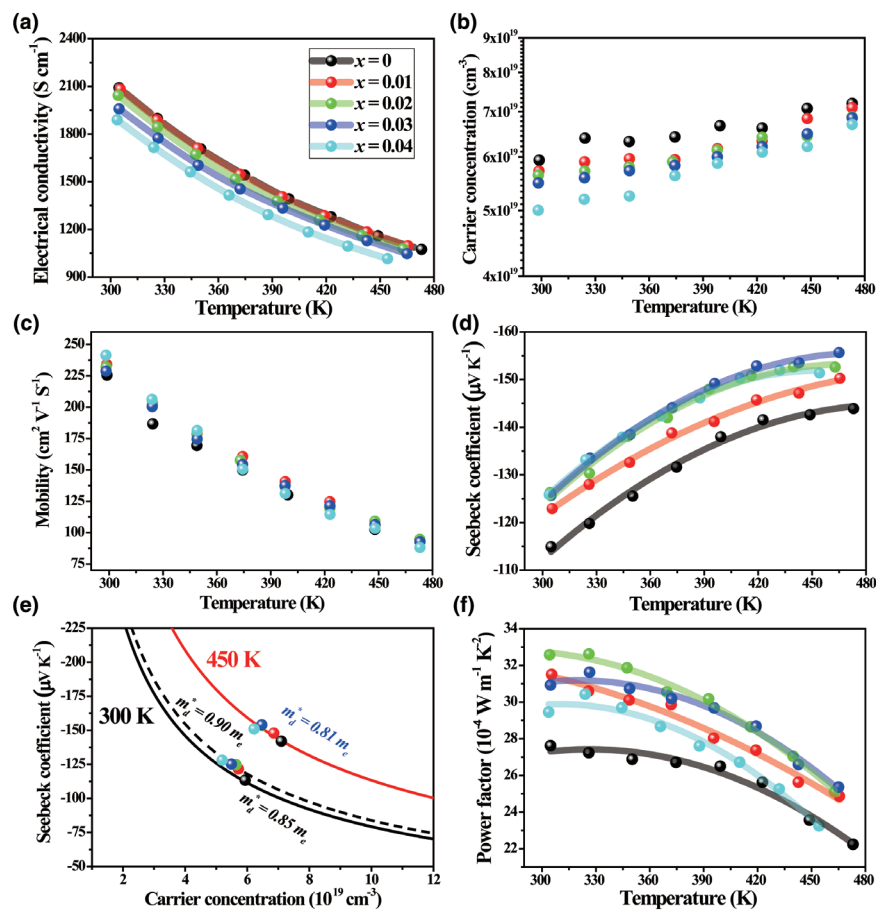
Figure 3. Temperature dependence of the a) electrical conductivity, b) carrier concentration, c) carrier mobility, d) Seebeck coefficient, and f) power factor of Bi$_2$Te$_3$–xFeTe$_2$ (x = 0, 0.01, 0.02, 0.03, and 0.04) samples. e) Pisarenko relations of Bi$_2$Te$_3$–xFeTe$_2$ (x = 0, 0.01, 0.02, 0.03, and 0.04) samples at 300 and 450 K.

Figure 3e, the S of x > 0 samples lying above the x = 0 Pisarenko line suggests that the band structure was modified by FeTe$_2$ incorporation. To further validate the effect of FeTe$_2$ incorporation on the band structure at high temperature (450 K), the S values of all samples (except x = 0.04) lie on the Pisarenko line, which suggests the negligible effect on the band structure by FeTe$_2$ incorporation at high temperature. However, the FeTe$_2$ incorporation does change the fermi level. At 300 K, the rate of the Seebeck coefficient increase with increasing x decreases (Figure 3d). When we compare the room temperature Seebeck coefficients of x = 0.03 and that of x = 0.04, they are almost identical. However, as the temperature increases, the Seebeck coefficient of x = 0.04 becomes lower than those of x = 0.03 and even x = 0.02 above 450 K. First of all, the Seebeck coefficient solely depends on the fermi level of the material. In other words, increasing x decreases the fermi level while increasing the Seebeck coefficient. As the x increases from 0.03 to 0.04, the drop in the fermi level is almost negligible at 300 K and that is the reason why we do not see much difference between the Seebeck coefficients of the x = 0.03 and 0.04. The reason that the Seebeck coefficient of the x = 0.04 is lower than those of x = 0.03 and 0.02 at high temperatures (>450 K) can be attributed to the increased bipolar conduction in the x = 0.04 sample. Accordingly, a larger enhancement in PF is achieved at a low temperature compared to a high temperature by controlling the band structure, which affects S and the carrier concentration, which dictates σ, as presented in Figure 3f.

the bandgap of the material that has comparable energy levels to the matrix, resulting in negligible energy offsets. In this case, the electrons would transfer through the interfaces without being scattered. Furthermore, these interfaces could trap low-energy electrons which could be the origin of the decrease in the carrier concentration.

Figure 3d shows the temperature-dependent S of the Bi$_2$Te$_3$-xFeTe$_2$ (x = 0, 0.01, 0.02, 0.03, and 0.04) samples. The S values of all samples are negative over the entire temperature range, indicating that electrons are the majority charge carriers in all samples, which agrees with the Hall measurements. The variation in S is consistent with the carrier concentration and σ. It is worth mentioning that the S increases with increasing FeTe$_2$ content up to x = 0.03 and then starts decreasing with a further increase in FeTe$_2$ content, over the entire temperature range. To understand the underlying mechanism of the increase in S, Pisarenko's relation (Equation 1) could give a valuable indication of the band structure modification.[41–44]

$$S = \frac{8\pi k_B^2}{3eh^2} m_d^* T \left(\frac{\pi}{3n}\right)^{\frac{2}{3}} \qquad (1)$$

where h is Planck constant, k_B is Boltzmann constant, m_d^* is the carrier effective mass, e is the electronic charge, and n is the electron concentration. By fitting Equation (1) at 300 K, as shown in

To further understand how the detailed atomic structure influences the transport properties, we calculated the electronic structure of a mixed-phase constructed by making an interface between Bi$_2$Te$_3$ and FeTe$_2$. To this end, we first used a supercell of two-unit cells of Bi$_2$Te$_3$ and 4-unit cells of FeTe$_2$ on top of Bi$_2$Te$_3$ (notice that the FeTe$_2$ cells have to be slightly contracted to adjust to the cells of Bi$_2$Te$_3$). We calculated the electronic structure (density of states, DOS, and projected density of states, PDOS) for Bi$_2$Te$_3$ and FeTe$_2$ at the equilibrium lattice constant of Bi$_2$Te$_3$. The results in Figure S2, Supporting Information, for relaxed configurations show that the mixed-phase is conductive (large DOS at the Fermi level) and this behavior is mainly governed by the interfacial strain due to the lattice mismatch between FeTe$_2$ and Bi$_2$Te$_3$. We then simulated the mixed structure at different lattice constants (relative to that of Bi$_2$Te$_3$), to check the effect of the biaxial strain. The minimum energy corresponds to a lattice constant of 11.697 Å, i.e., slightly expanded with respect to the equilibrium lattice constant of the Bi$_2$Te$_3$ supercell.

The contributions to the mixed-phase are shown in Figure S3, Supporting Information, at selected lattice constants, to verify the effect of the interfacial strain. As the lattice constant increases, i.e., the supercell is expanded, the PDOS looks more similar to the DOS of the pure

phases, although the Fermi level is not in an energy gap, but inside the valence band. Notice that the development of a large density of electronic states at the Fermi level is mainly due to the distortion induced by the interface formation. These results imply that $FeTe_2$ incorporation in Bi_2Te_3 influences the band structure of the matrix, which is consistent with the experimental results.

Next, we considered systems with larger unit cells along the direction perpendicular to the interface, i.e., 2- or 3-unit cells of Bi_2Te_3 and $FeTe_2$ along the z-direction, for three lattice constants around the equilibrium lattice constant as shown in the schematic (Figure S1, Supporting Information). The PDOS is shown in **Figure 4**. We also considered cases where the unit cell was displaced along the y-direction, but the results were very similar and no change was observed in the DOS, although the energy was considerably lower (various eV depending on the case). A general trend seen in Figure 4 is that, as the lattice constant increases, the DOS becomes sharper and higher around the Fermi level, especially due to the PDOS of $FeTe_2$. For the smaller lattice constant, as the size of the supercell along the z-direction increases, the DOS becomes smoother and smaller around the Fermi level, which seems to indicate that a larger fraction of pure phases in the mixed-phase gives a smaller DOS at the Fermi level, and hence, lower σ. The decrease in σ in the mixed-phase of $FeTe_2$ and Bi_2Te_3 (compared with that of the pure systems) is due to interfacial strain, where the major contribution comes from $FeTe_2$. Moreover, $FeTe_2$ is magnetic and due to magnetostriction, it prefers to maintain a larger volume in the magnetic state than in the non-magnetic case. When $FeTe_2$ forms a composite with Bi_2Te_3, Bi_2Te_3 tries to keep $FeTe_2$ as a smaller unit cell, whereas $FeTe_2$ prefers a larger volume. As a result, the $FeTe_2$–Bi_2Te_3 composite remains under stress and $FeTe_2$ induces strain in the composite system that reduces the DOS near the Fermi energy, which is expected to decrease σ.

2.3. Thermal Properties of Bi_2Te_3-$xFeTe_2$

The temperature-dependent κ_{tot} of Bi_2Te_3–$xFeTe_2$ ($x = 0$, 0.01, 0.02, 0.03, and 0.04) are presented in **Figure 5a**. Interestingly, the κ_{tot} values of the Bi_2Te_3–$0.01FeTe_2$ samples are lower by about 16% over the entire temperature range compared to those of the sample without $FeTe_2$. As discussed above, $\kappa_{tot} = \kappa_{lat} + \kappa_{ele}$. In addition to κ_{lat} and κ_{ele}, bipolar contributions to the thermal conductivity (κ_{bp}) become significant in narrow-gap TE materials like Bi–Te, especially at high temperatures. The observed upturns in the κ_{tot} curves of Bi_2Te_3–$xFeTe_2$ ($x = 0$, 0.01, 0.02, 0.03, and 0.04) samples at temperatures higher than 420 K originate from κ_{bp}. Thus, it is important to accurately estimate the role of κ_{ele} and κ_{bp} in these samples.

First, κ_{ele} is related to σ according to the Wiedemann–Franz relationship,[11] $\kappa_{ele} = L\sigma T$, where L is the Lorenz number/function, and in this work, it is calculated by assuming a single parabolic band and acoustic phonon scattering in the temperature range 300–470 K using the following relationships.[45]

$$S = \pm \frac{k_B}{e} \left[\frac{(r + 5/2)F_{r+3/2}(\xi)}{(r + 3/2)F_{r+1/2}(\xi)} - \xi \right] \quad (2)$$

$$F_n(\xi) = \int_0^\infty \frac{x^n}{1 + e^{(x-\xi)}} dx \quad (3)$$

$$L = \left(\frac{k_B}{e}\right)^2 \left[\frac{(r + 7/2)F_{r+5/2}(\xi)}{(r + 3/2)F_{r+1/2}(\xi)} - \left(\frac{(r + 5/2)F_{r+3/2}(\xi)}{(r + 3/2)F_{r+1/2}(\xi)}\right)^2 \right] \quad (4)$$

Here ξ, $F_n(\xi)$, and r are the reduced Fermi energy (E_F/k_BT), Fermi integral with nth order, and scattering parameter, respectively. Here, we used $r = -1/2$ for acoustic phonon scattering. Based on the above calculations, L values for all the samples were in the range of 1.71×10^{-8} $W\Omega K^{-2}$ to 1.84×10^{-8} $W\Omega K^{-2}$ over the whole temperature range. Secondly, κ_{bp} depends on individual electrical conductivity (σ_i) and Seebeck coefficient (S_i), where $i = CB$ or VB and is related to the conduction band (CB) and valence bands (VB) participating in transport, as presented in Equation (5).

$$\kappa_{bp} = \left[\sigma_{CB}S_{CB}^2 + \sigma_{VB}S_{VB}^2 - \frac{(S_{CB}\sigma_{CB} + S_{VB}\sigma_{VB})^2}{\sigma_{CB} + \sigma_{VB}} \right]T \quad (5)$$

However, experimentally decoupling band contributions from measured transport properties is virtually impossible. Instead, temperature-dependent σ_i and S_i were estimated using a two-band model.[46] Assuming that both the CB and VB are parabolic and carrier scattering is limited by acoustic phonon scattering, band parameters such as the DOS effective mass (m_i^* where $i = CB$, VB) and non-degenerate mobility related to the magnitude of carrier-phonon interaction ($\mu_{0,i}$ where $i = CB$, VB) for both CB and VB were fitted to experimental σ and S curves in Figure 3a,d. Then, σ_i and S_i in Equation (5) were calculated from the fitted m_i^* and $E_{def,i}$ to estimate κ_{bp}. See Supporting Information for details of the two-band model.

Figure 5b shows the pseudo-experimental κ_{lat} obtained by subtracting the calculated κ_{ele} and κ_{bp} from the measured κ_{tot} (symbols), and theoretical κ_{lat} computed using the Debye–Callaway model (lines).[47] Remarkably, the κ_{lat} decreased from ~ 0.60 $W\,m^{-1}\,K^{-1}$ for the sample with $x = 0$ to an extremely low value of ~ 0.47 $W\,m^{-1}\,K^{-1}$ for $x = 0.02$ at 372 K, which is a reduction of $\sim 27\%$. A possible explanation for this significant κ_{lat} reduction is the heterogeneous interfaces formed by $FeTe_2$ addition, as discussed above in the TEM results. However, when larger amounts of $FeTe_2$ were added ($x > 0.02$), κ_{lat} increased above that of the $x = 0.02$ sample. To understand the mechanism behind the phonon scattering via $FeTe_2$ incorporation, the theoretical κ_{lat} was fitted to the pseudo-experimental κ_{lat} using the Debye–Callaway model shown in Equation (6),

$$\kappa_{lat} = \frac{k_B}{2\pi^2 v} \left(\frac{k_BT}{\hbar}\right)^3 \int_0^{\theta_a/T} \frac{\tau_{tot}(z)\, z^4 e^z}{(e^z-1)^2} dz \quad (6)$$

The τ_{tot}, z, θ_a, v, k_B, and $\hbar$ in Equation (6) are the total phonon relaxation time, $\hbar\omega/k_BT$ (where ω is phonon angular frequency), Debye temperature, speed of sound, Boltzmann constant, and Planck's constant. The τ_{tot} depends on the individual phonon scattering mechanisms that are active for a specific defect structure of a material. For Bi_2Te_3–$xFeTe_2$ ($x = 0$, 0.01, 0.02, 0.03, and 0.04), τ_{tot} is as shown in Equation (7),

$$\tau_{tot}(z)^{-1} = \tau_U(z)^{-1} + \tau_B(z)^{-1} + \tau_{NP}(z)^{-1} \quad (7)$$

The τ_U, τ_B, and τ_{NP} in Equation (7) are the phonon relaxation time due to Umklapp phonon–phonon scattering (Umklapp scattering), boundary scattering (grain boundary scattering), and nanoparticle
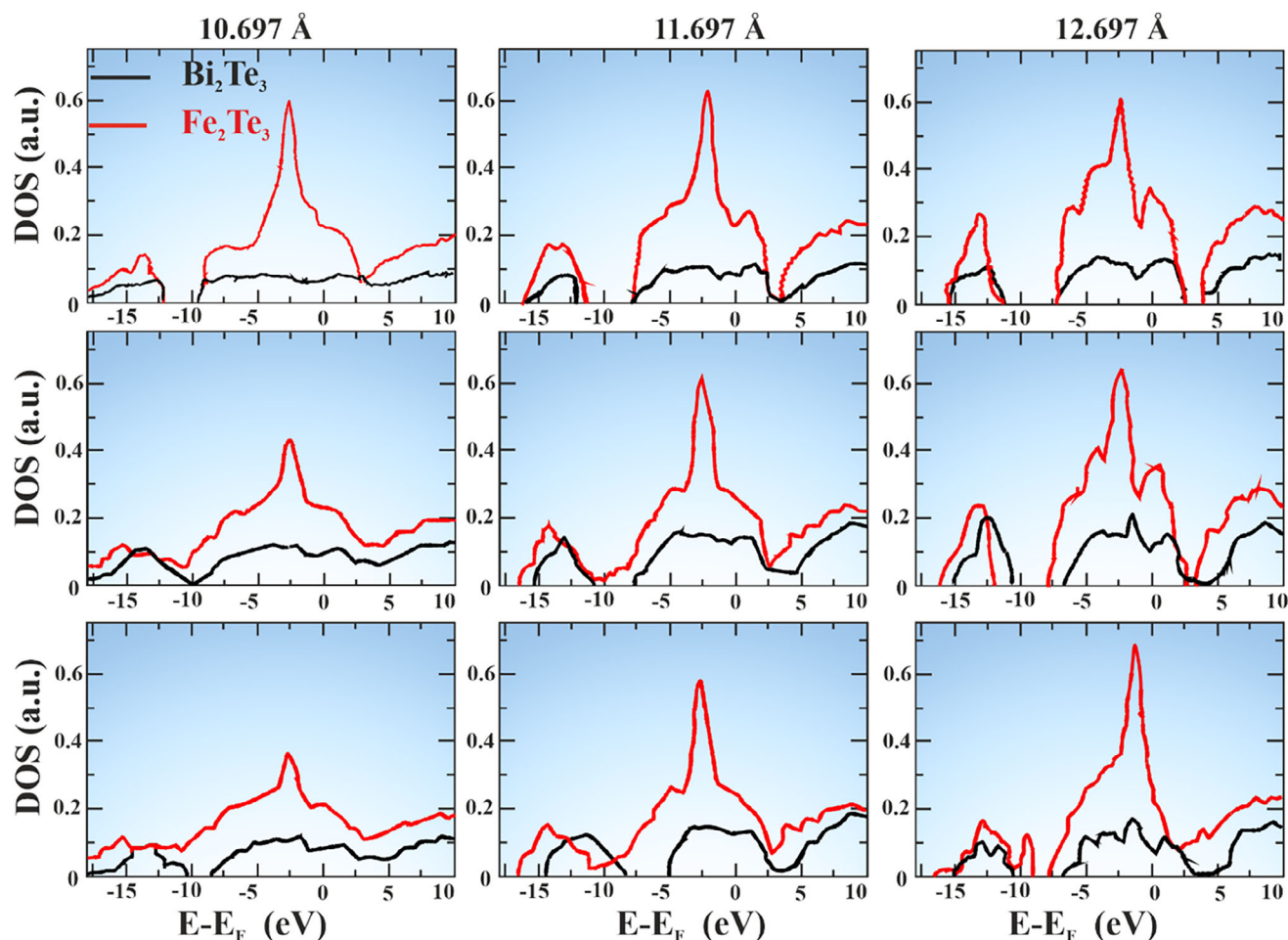
Figure 4. PDOS of Bi_2Te_3 and $FeTe_2$ for the mixed phase as a function of the lattice constant (from left to right) and the number of layers in the z-direction (from top to bottom).

scattering, respectively.[47] Because both TEM and density functional theory results suggest that the probability for atomic substitution (Fe doping) is small, phonon scattering due to point defects were neglected. For the $x = 0$ sample, the τ_{tot} required to calculate κ_{lat} was only estimated with τ_U and τ_B because no $FeTe_2$ nanoparticles were present in the sample (black line in Figure 5b). The τ_U and τ_B are provided in Equations (8) and (9) below.

$$\tau_U^{-1} = A_N \frac{2}{(6\pi^2)^{1/3}} \frac{k_B V^{1/3} \gamma^2 \omega^2 T}{M v^3} \qquad (8)$$

$$\tau_B^{-1} = \frac{v}{d} \qquad (9)$$

The terms A_N, V, γ, M, and d are the fitting parameters that account for normal phonon–phonon scattering, atomic volume, Grüneisen parameter, atomic mass, and grain size, respectively. Among these parameters, A_N is the only one that we fitted to the experimental κ_{lat}. For all Bi_2Te_3-$x(FeTe_2)$ ($x = 0$, 0.01, 0.02, 0.03, and 0.04) samples, the same A_N of 9.9 and d of 5 μm were adopted to calculate κ_{lat}. While keeping the same τ_U and τ_B, reasonable fits to the pseudo-experimental

κ_{lat} were achieved for $x > 0$ samples, as shown in Figure 5b. According to TEM results (Figure 2), two types of $FeTe_2$ incorporation were present in the samples: $FeTe_2$ particles (50–300 nm) and nano-precipitates (<50 nm). Only the phonon scattering due to $FeTe_2$ particles of 50–300 nm was included in the κ_{lat} calculations to minimize complexity, and the density of nano-precipitates was considered negligible. The phonon relaxation rate for nanoparticle scattering (τ_{NP}^{-1}) is

$$\tau_{NP}^{-1} = 2\pi R_{NP}^2 v\rho \qquad (10)$$

where, R_{NP} and ρ are the average size of the nanoparticle and the density of the nanoparticles, respectively. Because a higher τ_{NP}^{-1} corresponds to stronger phonon scattering, an increase in R_{NP} and ρ increase the phonon scattering intensity. Because the minimum size of the $FeTe_2$ particles was ∼50 nm, only the geometrical scattering via nanoparticles was considered.[48] For samples with $x \geq 0.01$, the R_{NP} and ρ extracted from fitting that was used to calculate κ_{lat} are given in **Table 1**. Compared to $x = 0.01$, the calculated ρ for $x = 0.02$ was higher, but both compositions have similar R_{NP}. However, for $x > 0.02$, R_{NP} increased significantly, with a corresponding reduction in ρ. Hence, the reduction in
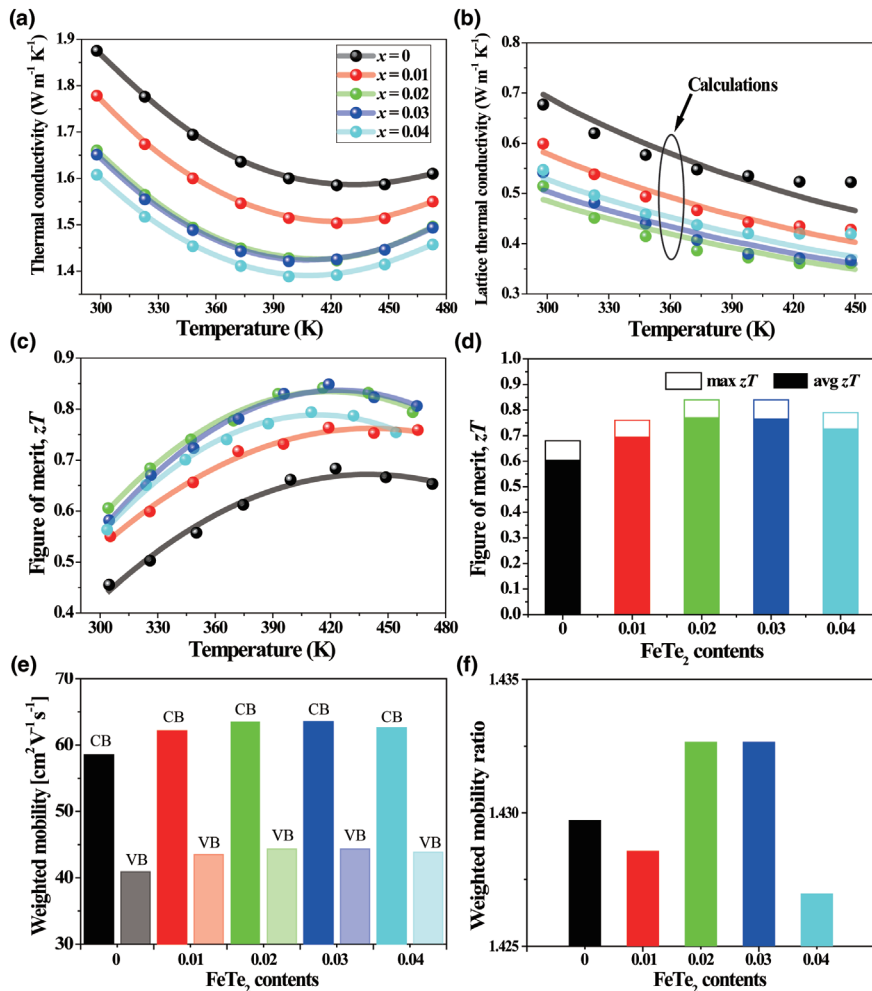
**Energy &
Environmental Materials**

Figure 5. Temperature dependence of the a) total thermal conductivity, b) lattice thermal conductivity, c) zT, d) average and maximum zT, e) weighted mobility, and f) weighted mobility ratio of Bi_2Te_3–$xFeTe_2$ ($x = 0$–0.04) samples.

ρ due to a significant increase in R_{NP} is responsible for the observed increase in κ_{lat} for $x \geq 0.03$. The fitted R_{NP} and ρ for different x are physically reasonable because the total volume of $FeTe_2$ ($\propto R_{NP}{}^3 \times \rho$) increases with increasing x. Experimentally, the increase in the size of the $FeTe_2$ is also confirmed from the $x = 0.02$ and 0.04 samples. While the average particle size of the $FeTe_2$ observed in the $x = 0.02$ sample is approximately 200 nm, that observed in the $x = 0.04$ sample amounts to 500 nm (Figure 2, Figure S9, Supporting Information).

Table 1. Average size (R_{NP}) and density (ρ) of $FeTe_2$ nanoparticles used to estimate the phonon relaxation rate for nanoparticle scattering in Bi_2Te_3–$xFeTe_2$ ($x = 0.01$–0.04).

Sample	R_{NP} (nm)	ρ (m^{-3})	$R_{NP}{}^3 \times \rho$
$x = 0.01$	270	1.5×10^{19}	0.30
$x = 0.02$	270	5.0×10^{19}	0.98
$x = 0.03$	360	2.3×10^{19}	1.07
$x = 0.04$	500	0.9×10^{19}	1.13

The temperature-dependent zT curves of the Bi_2Te_3–$xFeTe_2$ ($x = 0$–0.04) are shown in Figure 5c. Interestingly, despite their high σ, samples with $x = 0.02$ and 0.03 have the highest zT (0.84 at 416 K), which is 25% higher than that of the sample without $FeTe_2$ incorporation. It is worth mentioning that the maximum zT values of all $FeTe_2$-incorporated samples are higher over the entire temperature range tested. This is directly a result of the addition of appropriate amounts of $FeTe_2$, which can introduce a suitable quantity of electrons and defects that control the carrier concentration and lattice defects. Moreover, in addition to the power generating efficiency, the average zT (zT_{avg}) value over the entire temperature range is more significant than the maximum zT value that can be calculated over the experimental temperature range (room temperature-470 K) by integrating the area under the zT curves according to Equation (11),

$$zT_{avg} = \frac{1}{T_h - T_c} \int_{T_c}^{T_h} ZTdT \qquad (11)$$

Here, T_c and T_h are the cold- and hot-side temperatures, respectively. As shown in Figure 5d, the zT_{avg} values over the experimental temperature range were 0.60, 0.69, 0.77, 0.76, and 0.73 for $x = 0$, 0.01, 0.02, 0.03, and 0.04, respectively. The excellent performance of $FeTe_2$ incorporation in Bi_2Te_3 motivated us to further explore the origin and the possibility for further improvement.

Here, we estimated weighted mobility (μ_W) values of the CB and VB of Bi_2Te_3–$xFeTe_2$, and the results are shown in Figure 5e. The μ_W is determined as the product of μ_0 and $(m_d{}^*/m_e)^{3/2}$ (where m_e is the electron rest mass), and it is closely coupled to the optimum electronic performance of a TE material.[49] From the band parameters estimated using the two-band model (see Supporting Information for more details), the μ_W values for different $FeTe_2$ contents were obtained. The μ_W of the CB is approximately 40% higher than that of the VB for all $FeTe_2$ contents. Both μ_W of the CB and VB peak around $x = 0.02$ and 0.03, respectively. For narrow-band-gap materials like Bi_2Te_3, the weighted mobility ratio A (μ_W of the majority band divided by that of the minority band) needs to be considered in addition to the μ_W of an individual band due to bipolar conduction.[48] If A is high, the S rollover will be shifted to higher temperatures, and κ_{bp} will be low due to suppressed bipolar effects. Figure 5f shows A for different Bi_2Te_3–$xFeTe_2$ samples. Among the samples, those with $x = 0.02$ and 0.03 have the highest A, while $x = 0.04$ has the lowest A. Figure 3d,f shows that the $x = 0.03$ sample has the highest S and PF near 475 K. In contrast, the S of $x = 0.04$ drops rapidly with temperature, and its PF is the lowest at 450 K. In other words, samples with $x = 0.02$ and 0.03 with high A will have excellent electronic performance at high temperatures. Because the $x = 0.02$ and 0.03 samples also have the lowest κ_{lat}, their
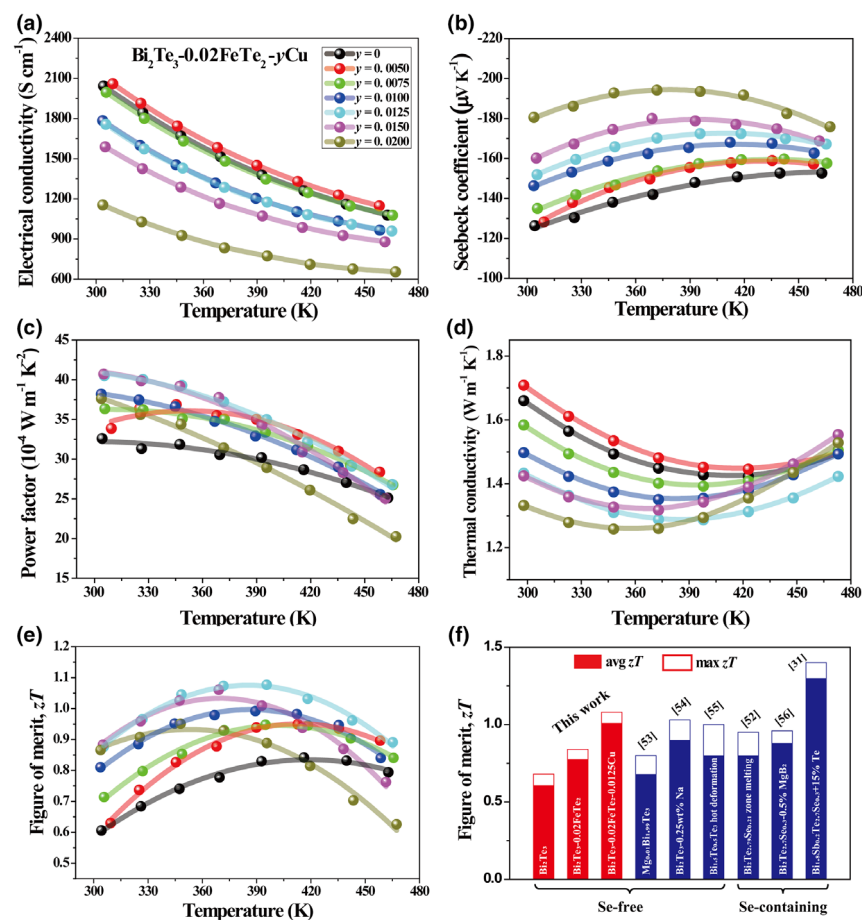
Figure 6. Temperature dependence of the a) electrical conductivity, b) Seebeck coefficient, c) power factor, d) total thermal conductivity, e) zT, and f) average and maximum zT comparison for n-type Bi$_2$Te$_3$-based TE materials.[31,52–56]
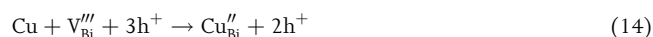
experimental zT values at 475 K are the highest among all samples (Figure 5c).

2.4. Cu Doping on Bi$_2$Te$_3$–0.02FeTe$_2$

The zT values for n-type Bi$_2$Te$_3$ TE materials were increased after FeTe$_2$ incorporation regardless of the composition. Benefitting from the lowest κ_{lat} and relatively high σ of the $x = 0.02$ sample, further enhancement in the TE performance was attempted through carrier optimization. Since it was predicted that the peak zT of Bi$_2$Te$_3$-based materials lies in the carrier concentration range of ~ 2×10^{19} cm^{-3}, which is lower than that of our optimum ($x = 0.02$) sample ~ 5.6×10^{19} cm^{-3}.[50] Therefore, these results motivated us to further tune the carrier concentrations by acceptor doping. For this purpose, the $x = 0.02$ content was fixed in Bi$_2$Te$_3$–xFeTe$_2$ and the Cu was incorporated for the subsequent investigations.

Figure 6a shows the temperature dependence of σ for Bi$_2$Te$_3$–0.02FeTe$_2$–yCu ($y = 0$–0.02). It is interesting to see that for the sample with a small amount of Cu ($y = 0.0050$), the σ increased slightly compared to the original composition, while for the heavily doped samples ($y \geq 0.0075$) the opposite trend was observed, as expected. To understand this behavior, temperature-dependent Hall measurements were

performed. It is interesting to see that carrier concentration decreases systematically over the entire temperature range with increasing Cu content, as shown in Figure S6a, Supporting Information. Moreover, the mobility of the samples increases with increasing Cu content up to $y = 0.0125$ and then decreases with a further increase in Cu content, as shown in Figure S6b, Supporting Information. To understand the mechanism of Cu doping in Bi$_2$Te$_3$–0.02FeTe$_2$, which leads to p-type and n-type conduction, we first need to understand the defect mechanism in Bi$_2$Te$_3$-based systems. For this purpose, we considered a $2 \times 2 \times 2$ supercell of Bi$_2$Te$_3$ and investigated the following defects: (i) Te vacancy, V$_{Te}$; (ii) Te anti-site, Te$_{Bi}$, where Te is substituted into a Bi site; (iii) Te$_{Bi}$ + V$_{Te}$; (iv) Bi vacancy, V$_{Bi}$; (v) Bi anti-site, Bi$_{Te}$, where Bi is doped at a Te site; and (vi) Bi$_{Te}$ + V$_{Bi}$. The analysis of the calculated electronic structures of the above defects shows that the V$_{Te}$ case induces a hole band on top of the VB. Similarly, for the Te$_{Bi}$ case, the Fermi level is inside the CB edge, and electron pockets at the Γ point were observed. Thus, the Te$_{Bi}$ defect in Bi$_2$Te$_3$ behaves as an n-type degenerate semiconductor. For the Te$_{Bi}$ + V$_{Te}$ system, some hole and electron bands were observed, i.e., a compensated semiconductor. The V$_{Bi}$ case also induces holes and a hole band on top of the VB. Similarly, for the Bi$_{Te}$ case, the Fermi level is inside the VB, and this system is a kind of p-type degenerate semiconductor. However, for the Bi$_{Te}$ + V$_{Bi}$ system, the bandgap is reduced to 0.045 eV at the Z point, so this system behaves as a narrow-bandgap semiconductor. Overall, this mechanism can be understood by the defect reactions shown in Equations (12) and (13). We dealt with Te-rich Bi$_2$Te$_3$, consequently, Te$_{Bi}$ should be the dominant defect rather than Bi$_{Te}$.

$$Bi_{Bi} + Te_{Te} \rightarrow Te^{\bullet}_{Bi} + V^{\bullet\bullet}_{Te} + 3e^- \tag{12}$$

$$Bi_{Bi} + Te_{Te} \rightarrow Bi'_{Te} + V'''_{Bi} + 4h^+ \tag{13}$$

$$Cu + V'''_{Bi} + 3h^+ \rightarrow Cu''_{Bi} + 2h^+ \tag{14}$$

$$Cu + V^{\bullet\bullet}_{Te} + 2e^- \rightarrow Cu^{\bullet}_i + e^- \tag{15}$$

Based on the above observations, the mechanism of Cu doping in Bi$_2$Te$_3$–0.02FeTe$_2$ can be elucidated by two possible assumptions. First, Cu atoms substitute at Bi sites (Cu$_{Bi}$) and act as a p-type acceptor according to Equation (14). In this case, electron generation would be suppressed by hole generation, and the carrier concentrations subsequently decrease. Second, the Cu atom enters into the interstitial sites in the crystal lattice (Cu$_i$) and makes Cu$_i$ the dominant defect rather than Cu$_{Bi}$. As discussed above, in the case of Te-rich Bi$_2$Te$_3$, Te$_{Bi}$ is the dominant defect, but Cu$_i$ defects can possibly suppress the formation of Te$_{Bi}$. This mechanism would decrease the net carrier concentration of Bi$_2$Te$_3$

because Cu doping reduces the generation of electrons by reducing the concentration of Te_{Bi} defects. It should be noted that once the solubility limit of Cu is exceeded, the formation of a pseudo-binary phase can be formed by the Cu migration inside the Bi_2Te_3 matrix, affecting thermal and electrical transport properties. However, in our case, it is believed that the solubility limit of Cu has not yet been reached.[51] In addition, we performed TEM analysis on the Cu-doped sample (Bi_2Te_3–0.02$FeTe_2$–0.0125Cu) to investigate the possibility of secondary phase formation induced by Cu doping. The HRTEM (Figure S10a, Supporting Information) and corresponding FFT pattern (Figure S10b, Supporting Information) confirm the presence of $FeTe_{0.9}$ nanoprecipitate in the Cu-doped sample. A small amount of Cu was detected within the nanoprecipitate from the EDS line scan result (Figure S10c, Supporting Information), but it did not affect the structure of the precipitate. It is noted that the Fe-Te based secondary phase is formed in the sample regardless of Cu doping. Furthermore, the Cu doping does not induce the formation of any Cu-related secondary phases.

Figure 6b shows the temperature dependence of S for Bi_2Te_3–0.02$FeTe_2$–yCu (y = 0–0.02) samples with n-type conduction for all samples over the entire temperature range. Moreover, S decreases systematically with increasing Cu content, which is similar to the variation in the carrier concentration. It is worth noting that at high temperature, the absolute value of S decreases with increasing temperature, which is attributed to the bipolar effect and wide shoulder of the $S(T)$ shift to lower temperature with increasing Cu content. When optimizing TE materials by doping, it is usually observed that zT increases with doping concentration until bipolar effects become active at high doping concentrations and thereafter limit the performance. The PF will go through a maximum and then fall off and bipolar effects will increase κ_{ele} and ultimately reduce zT. This suggests that the optimal carrier concentration in this work is achieved with less than 2 at% Cu atoms. Owing to the optimized carrier concentration (0.0125 Cu), a noticeably high PF of $\sim 41 \times 10^{-4}$ W m^{-1} K^{-2} was obtained, which is 27% higher than that of the sample without Cu doping (Figure 6c). Note that the PF of the optimized composition is comparable to that of zone-melted $Bi_2Te_{2.79}Se_{0.21}$ ingot.[52] This enhanced PF is attributed to the combination of an increase in S and an optimal σ. In addition to the noticeably higher PF, the optimization of the carrier concentration substantially reduces κ_{ele} (corresponding to the reduced σ through Cu doping). Using the Equations (2)–(4), L, κ_{lat}, and κ_{ele} were calculated; markedly reduced κ_{ele} was observed as the Cu-doped samples have much lower κ_{tot} than the undoped material (Figure 6d).

Benefitting from the simultaneously higher PF and reduced κ_{tot}, the zT of the Cu-doped samples substantially increased (Figure 6e). Overall, zT_{max} increases from ~ 0.68 for Bi_2Te_3 to 0.83 for Bi_2Te_3–0.02$FeTe_2$, and ~ 1.08 in Bi_2Te_3–0.02$FeTe_2$–0.0125Cu at 395 K, accordingly. The zT_{avg} value in the temperature range of 300–470 K enhances dramatically for optimal Cu doping (Figure 6f), where zT_{avg} value increases $\sim 68\%$ compared to pristine Bi_2Te_3 (~ 0.60 for Bi_2Te_3, ~ 1.01 for Bi_2Te_3–0.02$FeTe_2$–0.0125Cu). This value is the highest achieved so far for an n-type Se-free Bi_2Te_3 system, which is comparable to most Se-containing $Bi_2Te_{2.7}Se_{0.3}$ systems.[31,52–56] Our approach could provide a facile strategy to enhance the TE performance of various matrix materials, and we expect a higher TE performance through additional texturing techniques such as hot deformation. Further, exploring the possibility of introducing other types of nanoinclusions and dopants could lead to further enhancement of the thermoelectric performance of Bi_2Te_3-based thermoelectric materials. The developed thermoelectric device could be integrated with other p-type materials to measure the

conversion efficiency and improve their overall performance. With this progress, materials could be used in a broad spectrum of energy harvesting and waste heat recovery applications, contributing to the sustainable development of society. Further efforts could be made the long-term durability and to improve the stability of the device, as well as to optimize the cost-efficiency of the synthesis process. The next step would be to intensify the synthesis process and explore potential commercial applications of these materials, such as recovering residual heat in automotive or industrial environments.

3. Conclusion

In summary, we have achieved a significant improvement in the TE performance of Se-free Bi_2Te_3-based TE material using facile processes including melt spinning and spark plasma sintering. The spontaneously generated $FeTe_2$ nanoinclusions reduce the lattice thermal conductivity and significantly increase the Seebeck coefficient. In addition, the Cu doping in Bi_2Te_3–0.02$FeTe_2$ as an accepter considerably enhances PF, where the optimum composition of Bi_2Te_3–0.02$FeTe_2$–0.0125Cu gives a maximum zT value of 1.08 at 395 K, which is 60% higher than that of the pristine Bi_2Te_3 materials. Most importantly, the zT_{avg} increased from ~ 0.60 (Bi_2Te_3) to ~ 1.01 (Bi_2Te_3–0.02$FeTe_2$–0.0125Cu) in the temperature range of 300–470 K relevant for low-temperature waste-heat recovery. Overall, this study could provide a facile approach of spontaneous nanoinclusion structure (without any additional process) and achieving high zT using a Se-free TE material that has promising potential for TE commercialization in terms of stability and performance.

4. Experimental Section

Experimental details: For the synthesis of Bi_2Te_3–xFeTe_2 (x = 0, 0.01, 0.02, 0.03, and 0.04) and Bi_2Te_3–0.02$FeTe_2$–yCu (y = 0–0.02) ingots, high-purity elements ($>99.99\%$) were used as starting materials. Mixtures of raw materials were sealed in a vacuum quartz ampule and heated to 1373 K for 4 h followed by a dwell at 973 K for 6 h and then quenching in cold water. The ingots were then placed in a graphite nozzle with a 0.4 mm diameter in an induction heater for an MS process, and the rotating speed of the Cu wheel was optimized to $1120 \times g$. Thin ribbons were formed by the MS process, which had an amorphous structure on the contact surface and crystalline nanostructure on the free surface. The melt-spun ribbons were roughly pulverized into powders and sintered using SPS at 773 K for 3 min under 60 MPa. The crystal structure of the sintered pellets was determined by XRD (New D8 Advance, Bruker, Cu Kα), and the microstructure of the composites were investigated by SEM (JSM-7600F, JEOL) with EDS. A thin sample was prepared by mechanical polishing followed by Ar ion milling (PIPS, Gatan Corporation). For the microstructural analysis, a scanning TEM system (Titan 80–300, FEI Corporation) equipped with a Cs probe corrector and EDS was used. The chemical states of nanoinclusions were analyzed by XPS measurement. The σ and S were measured from room temperature to 473 K using a four-point-probe measurement system (ZEM-3, ULVAC-RIKO), and the thermal diffusivity values were measured by a laser-flash analysis method (TA Instruments, DLF 1300). The carrier concentrations and mobilities were measured using a Hall measurement system (HT-Hall, ResiTest 8300, Toyo Corporation). The uncertainties in all of our data were less than 5%.

Simulations: Density functional theory simulations were performed with the SIESTA code. We used a double-zeta polarized basis set and a real-space mesh defined with a plane-wave cutoff value of 300 Ry. We employed GGA, as well as the GGA + U functional with a U term of 5.0 eV for the d orbitals of Fe to correctly describe the electronic structure of $FeTe_2$ and $FeTe_2$–Bi_2Te_3. We relaxed the atomic positions until all forces were smaller than 0.05 eVÅ^{-1}, and the unit cell was relaxed until the stress was smaller than 1 GPa. Our GGA optimized values

of lattice parameters of marcasite FeTe$_2$ are $a = 5.33$ Å; $b = 6.25$ Å; $c = 3.84$ Å, which agree with the experimental values of $a = 5.275$ Å; $b = 6.269$ Å; $c = 3.872$ Å. Our optimized values for Bi$_2$Te$_3$ are $a = 4.40$; $c = 30.89$. These numerical values illustrate the accuracy of our computational parameters. We first calculated the electronic structure (DOS and bands) of the undoped materials. The GGA + U calculated bandgap of FeTe$_2$ is 0.33 eV, which is comparable with previous works.[57] We stress that GGA cannot correctly describe the electronic structure of FeTe$_2$ and the inclusion of U is necessary in this case. The GGA calculated bandgap of Bi$_2$Te$_3$ is 0.32 eV. This implies that strong correlations are most important in FeTe$_2$.

Acknowledgements

Conflict of Interest

The authors declare no conflict of interest.

Supporting Information

Supporting Information is available from the Wiley Online Library or from the author.

Keywords

[1] S. Boccardi, F. Ciampa, M. Meo, *Smart Mater. Struct.* **2019**, 28, 105057.

[2] R. Freer, A. V. Powell, *J. Mater. Chem. C* **2020**, 8, 441.

[3] T. Cao, X.-L. Shi, Z.-G. Chen, *Prog. Mater. Sci.* **2023**, 131, 101003.

[4] B. Hu, X.-L. Shi, J. Zou, Z.-G. Chen, *Chem. Eng. J.* **2022**, 437, 135268.

[5] W.-Y. Chen, X.-L. Shi, J. Zou, Z.-G. Chen, *Mater. Sci. Eng. R Rep.* **2022**, 151, 100700.

[6] Z.-H. Zheng, X.-L. Shi, D.-W. Ao, W.-D. Liu, M. Li, L.-Z. Kou, Y.-X. Chen, F. Li, M. Wei, G.-X. Liang, P. Fan, G. Q. Lu, Z.-G. Chen, *Nat. Sustain.* **2022**, 6, 180.

[7] L. D. Zhao, V. P. Dravid, M. G. Kanatzidis, *Energ. Environ. Sci.* **2014**, 7, 251.

[8] T. M. Tritt, M. A. Subramanian, *MRS Bull.* **2006**, 31, 188.

[9] J. U. Rahman, N. V. Du, W. H. Nam, W. H. Shin, K. H. Lee, W. S. Seo, M. H. Kim, S. Lee, *Sci. Rep.* **2019**, 9, 8624.

[10] N. Van Du, J. U. Rahman, P. T. Huy, W. H. Shin, W.-S. Seo, M. H. Kim, S. Lee, *Acta Mater.* **2019**, 166, 650.

[11] C. Kittel, *Introduction to Solid State Physics*, John Wiley & Sons, Hoboken **2005**.

[12] E. Flage-Larsen, O. Prytz, *Appl. Phys. Lett.* **2011**, 99, 202108.

[13] H.-S. Kim, Z. M. Gibbs, Y. Tang, H. Wang, G. J. Snyder, *APL Mater.* **2015**, 3, 041506.

[14] J. U. Rahman, E.-J. Meang, D. Nguyen, W.-S. Seo, A. Hussain, M. H. Kim, S. Lee, *J. Electron. Mater.* **2017**, 3, 1740.

[15] H. Mun, S. M. Choi, K. H. Lee, S. W. Kim, *ChemSusChem* **2015**, 8, 2312.

[16] S. I. Kim, K. H. Lee, H. A. Mun, H. S. Kim, S. W. Hwang, J. W. Roh, D. J. Yang, W. H. Shin, X. S. Li, Y. H. Lee, G. J. Snyder, S. W. Kim, *Science* **2015**, 348, 109.

[17] C. Xinzhi, F. Xi'an, R. Zhenzhou, Y. Fan, G. Zhanghua, L. Guangqiang, *J. Phys. D Appl. Phys.* **2014**, 47, 115101.

[18] J. S. Yoon, J. M. Song, J. U. Rahman, S. Lee, W. S. Seo, K. H. Lee, S. Kim, H. S. Kim, S. I. Kim, W. H. Shin, *Acta Mater.* **2018**, 158, 289.

[19] J. Martin, L. Wang, L. Chen, G. S. Nolas, *Phys. Rev. B* **2009**, 79, 115311.

[20] Y. Y. Li, X. Y. Qin, D. Li, J. Zhang, C. Li, Y. F. Liu, C. J. Song, H. X. Xin, H. F. Guo, *Appl. Phys. Lett.* **2016**, 108, 62104.

[21] J. Choi, J. Y. Lee, S. S. Lee, C. R. Park, H. Kim, *Adv. Energy Mater.* **2016**, 6, 1502181.

[22] T. H. Zou, X. Y. Qin, D. Li, B. J. Ren, G. L. Sun, Y. C. Dou, Y. Y. Li, L. L. Li, J. Zhang, H. X. Xin, *J. Appl. Phys.* **2014**, 115, 53710.

[23] Y. Ma, Q. Hao, B. Poudel, Y. Lan, B. Yu, D. Wang, G. Chen, Z. Ren, *Nano Lett.* **2008**, 8, 2580.

[24] M. Jeong, J. Y. Tak, S. Lee, W. S. Seo, H. K. Cho, Y. S. Lim, *J. Alloys Compd.* **2017**, 696, 213.

[25] W. Zhao, Z. Liu, Z. Sun, Q. Zhang, P. Wei, X. Mu, H. Zhou, C. Li, S. Ma, D. He, P. Ji, W. Zhu, X. Nie, X. Su, X. Tang, B. Shen, X. Dong, J. Yang, Y. Liu, J. Shi, *Nature* **2017**, 549, 247.

[26] T. Zhu, Y. Liu, C. Fu, J. P. Heremans, J. G. Snyder, X. Zhao, *Adv. Mater.* **2017**, 29, 1605884.

[27] R. T. Delves, A. E. Bowley, D. W. Hazelden, H. J. Goldsmid, *Proc. Phys. Soc.* **1961**, 78, 838.

[28] Y. Pan, J.-F. Li, *NPG Asia Mater.* **2016**, 8, e275.

[29] B. Zhu, Y. Yu, X. Y. Wang, F. Q. Zu, Z. Y. Huang, *J. Mater. Sci.* **2017**, 52, 8526.

[30] J. M. Song, J. U. Rahman, J. Y. Cho, S. Lee, W. S. Seo, S. Kim, S.-I. Kim, K. H. Lee, D. Roh, W. H. Shin, *Scr. Mater.* **2019**, 165, 78.

[31] B. Zhu, X. Liu, Q. Wang, Y. Qiu, Z. Shu, Z. Guo, Y. Tong, J. Cui, M. Gu, J. He, *Energ. Environ. Sci.* **2020**, 13, 2106.

[32] W.-S. Liu, Q. Zhang, *Energy Mater.* **2011**, 1, 577.

[33] G. C. Wei, J. R. Keiser, R. S. Crouse, M. D. Allen, A. C. Schaffhauser, Post-test analysis of components from selenide isotope generator modules M-7, M-15, and M-18, ORNL/TM--6826. **1979**.

[34] D. R. Brown, T. Day, T. Caillat, G. J. Snyder, *J. Electron. Mater.* **2013**, 42, 2014.

[35] J. Horák, Z. Star, J. Votinsk, *Philos. Mag. B* **1994**, 69, 31.

[36] J. Horák, Z. Stary, P. Lošťák, J. Pancíř, *J. Phys. Chem. Solid* **1990**, 51, 1353.

[37] J. C. Slater, *J. Chem. Phys.* **1964**, 41, 3199.

[38] B. Jariwala, D. Shah, N. M. Ravindra, *Thin Solid Films* **2015**, 589, 396.

[39] E. P. Arévalo-López, P. Romero-Moreno, J. L. Rosas-Huerta, L. Huerta, C. Minaud, M. L. Marquina, R. Escamilla, M. Romero, *J. Alloys Compd.* **2022**, 899, 163297.

[40] W. H. Shin, J. W. Roh, B. Ryu, H. J. Chang, H. S. Kim, S. Lee, W. S. Seo, K. Ahn, *ACS Appl. Mater. Interfaces* **2018**, 10, 3689.

[41] G. J. Snyder, E. S. Toberer, *Nat. Mater.* **2008**, 7, 105.

[42] A. F. Ioffe, *Physics of Semiconductors*, Academic Press, New York **1960**.

[43] E. Lee, J. Ko, J. Y. Kim, W. S. Seo, S. M. Choi, K. H. Lee, W. Shim, W. Lee, *J. Mater. Chem. C* **2016**, 4, 1313.

[44] J. U. Rahman, N. Van Du, G. Rahman, V. M. Garcia-Suarez, W. S. Seo, M. H. Kim, S. Lee, *RSC Adv.* **2017**, 7, 53255.

[45] A. F. May, G. J. Snyder, *Materials, Preparation, and Characterization in Thermoelectrics*, CRC Press, Boca Raton **2017**, p. 11.

[46] M. Kim, S. I. Kim, S. W. Kim, H. S. Kim, K. H. Lee, *Adv. Mater.* **2021**, 33, 2005931.

[47] H. S. Kim, S. D. Kang, Y. L. Tang, R. Hanus, G. J. Snyder, *Mater. Horiz.* **2016**, 3, 234.

[48] K. H. Lee, Y.-M. Kim, C. O. Park, W. H. Shin, S. W. Kim, H.-S. Kim, S.-I. Kim, *Mater. Today Energy* **2021**, 21, 100795.

[49] I. T. Witting, T. C. Chasapis, F. Ricci, M. Peters, N. A. Heinz, G. Hautier, G. J. Snyder, *Adv. Electron. Mater.* **2019**, 5, 1800904.

[50] Q. Zhang, T. Fang, F. Liu, A. Li, Y. Wu, T. Zhu, X. Zhao, *Chem. Asian J.* **2020**, *15*, 2775.

[51] Q. Lognoné, F. Gascoin, *J. Alloys Compd.* **2014**. DOI: https://doi.org/10.1016/j.jallcom.2014.04.166

[52] L. Hu, H. Wu, T. Zhu, C. Fu, J. He, P. Ying, X. Zhao, *Adv. Energy Mater.* **2015**, *5*, 1500411.

[53] S. Byun, J. Cha, C. Zhou, Y. K. Lee, H. Lee, S. H. Park, W. B. Lee, I. Chung, *J. Solid State Chem.* **2019**, *269*, 396.

[54] L.-Y. Lou, J. Yang, Y.-K. Zhu, H. Liang, Y.-X. Zhang, J. Feng, J. He, Z.-H. Ge, L.-D. Zhao, *Adv. Sci.* **2022**, *9*, 2203250.

[55] Y. Zhou, F. Meng, J. He, A. Benton, L. Hu, F. Liu, J. Li, C. Zhang, W. Ao, H. Xie, *ACS Appl. Mater. Interfaces* **2020**, *12*, 31619.

[56] B. Chen, J. Li, M. Wu, L. Hu, F. Liu, W. Ao, Y. Li, H. Xie, C. Zhang, *ACS Appl. Mater. Interfaces* **2019**, *11*, 45746.

[57] X.-H. Tian, J.-M. Zhang, *Superlattice. Microst.* **2018**, *119*, 201.